Electron currents and heating in the ion diffusion region of asymmetric reconnection

D. B. Graham[1], Yu. V. Khotyaintsev[1], C. Norgren[1,2], A. Vaivads[1], M.

André[1], P.-A. Lindqvist[3], G. T. Marklund[3], R. E. Ergun[4], W. R. Paterson[5],

D. J. Gershman[5,6], B. L. Giles[5], C. J. Pollock[5], J. C. Dorelli[5], L. A.

Avanov[5,6], B. Lavraud[7], Y. Saito[8], W. Magnes[9], C. T. Russell[10], R. J.

Strangeway[10], R. B. Torbert[11], and J. L. Burch[12]

———————

[1]Swedish Institute of Space Physics,

Uppsala, Sweden.

[2]Department of Physics and Astronomy,

Uppsala University, Uppsala, Sweden

[3]KTH Royal Institute of Technology,

Stockholm, Sweden.

In this letter the structure of the ion diffusion region of magnetic reconnection at Earth's magnetopause is investigated using the Magnetospheric

[4]Laboratory of Atmospheric and Space

Physics, University of Colorado, Boulder,

CO, USA.

[5]NASA Goddard Space Flight Center,

Greenbelt, MD, USA.

[6]University of Maryland, College Park,

MD, USA.

[7]IRAP, CNRS, Toulouse, France.

[8]Institute of Space and Astronautical

Science, JAXA, Sagamihara, Japan.

[9]Space Research Institute, Austrian

Academy of Sciences, Graz, Austria

[10]University of California, Los Angeles,

CA, USA.

[11]University of New Hampshire, Durham,

NH, USA.

[12]Southwest Research Institute, San

Antonio, TX, USA.

Multiscale (MMS) spacecraft. The ion diffusion region is characterized by a strong DC electric field, approximately equal to the Hall electric field, intense currents, and electron heating parallel to the background magnetic field. Current structures well below ion spatial scales are resolved and the electron motion associated with lower-hybrid drift waves is shown to contribute significantly to the total current density. The electron heating is shown to be consistent with large-scale parallel electric fields trapping and accelerating electrons, rather than wave-particle interactions. These results show that sub-ion scale processes occur in the ion diffusion region and are important for understanding electron heating and acceleration.

1. Introduction

Magnetic reconnection is a fundamental process in solar and astrophysical plasmas. Magnetic reconnection transforms magnetic field energy into particle energy by rearranging the magnetic field topology. Magnetic field lines are known to reconnect in regions where ions and then electrons (on smaller spatial scales) become demagnetized and are no longer frozen in; the ion and electron diffusion regions, respectively. Within the ion diffusion region electrons and ions undergo different motion as the ions become demagnetized, resulting in electric currents, which produce the Hall electric field. For symmetric reconnection, where the reconnecting plasmas have the same properties, the ion diffusion region is characterized by quadrupolar Hall magnetic fields, dipolar Hall electric field [*Vaivads et al.*, 2004a], and electron heating parallel to **B** [*Egedal et al.*, 2008].

At Earth's magnetopause the reconnecting magnetospheric and magnetosheath plasmas typically have distinct properties, making magnetic reconnection highly asymmetric. Asymmetries in the densities and magnetic field strengths of reconnection plasmas are known to distort the large-scale structure of reconnection; in particular, the Hall magnetic and electric fields become dipolar and unipolar, respectively [*Mozer et al.*, 2008; *Tanaka et al.*, 2008]. In both symmetric and asymmetric reconnection the ion diffusion region is characterized by strong electron heating parallel to **B** [*Chen et al.*, 2008; *Graham et al.*, 2014]. This heating is argued to be produced by large-scale parallel electric fields, which trap and accelerate electrons [*Egedal et al.*, 2008]. However, wave-particle interactions may also play an important role in electron heating and acceleration. In particular, lower-hybrid drift waves are well known to develop at sharp density gradients [*Krall and*

Liewer, 1971], such as the magnetopause, and can heat electrons [*Cairns and McMillan*, 2005]. Observations and simulations show that intense electrostatic lower-hybrid waves develop in the magnetospheric separatrices [*Bale et al.*, 2002; *Vaivads et al.*, 2004b; *Pritchett*, 2013], but only electromagnetic lower-hybrid waves are expected to develop near the X line [*Roytershteyn et al.*, 2012].

The processes operating at electron spatial scales have been difficult to observe and particle detectors have lacked the cadence required to investigate particle dynamics at these scales. In this letter we investigate the ion diffusion region of asymmetric magnetic reconnection using the Magnetospheric Multiscale (MMS) mission. MMS is specifically designed to investigate processes operating at electron spatial scales [*Burch et al.*, 2015]. We use MMS to investigate the structure and properties of the ion diffusion region at Earth's magnetopause, focusing on the structure of the electric fields, current sheets, and the processes responsible for electron heating and acceleration.

2. Observations

In this letter we use data from the MMS spacecraft; we use magnetic field **B** data from the Fluxgate Magnetometer (FGM) [*Russell et al.*, 2014] and the Search Coil Magnetometer (SCM) [*Le Contel et al.*, 2014], electric field **E** data from the Electric field Double Probes (EDP) [*Lindqvist et al.*, 2014; *Ergun et al.*, 2014], and particle data from the Fast Plasma Investigation (FPI) [*Pollock et al.*, 2016]. We use **E** data sampled at $32\,\mathrm{s}^{-1}$ (fast mode) and $8192\,\mathrm{s}^{-1}$ (burst mode). The three-dimensional electron distributions are sampled at $33\,\mathrm{s}^{-1}$ by FPI. We investigate the magnetopause crossing observed on 30 October 2015 between 05:15:00 UT and 05:17:00 UT. The vector data are presented

in Geocentric Solar Ecliptic (GSE) coordinates, unless otherwise stated. During this interval the spacecraft were in a tetrahedral configuration and separated by $\sim 15\,\text{km}$, ideal for investigating processes at sub-ion spatial scales. We present an overview of the event and investigate the electric fields, current sheets, and electron heating in the ion diffusion region.

2.1. Overview

An overview of this magnetopause crossing observed by MMS1 is presented in Figure 1. The magnetopause crossing from the magnetosphere to the magnetosheath is observed between 05:15:45 UT and 05:15:50 UT and is characterized by a reversal in B_z and an increase in the electron number density n_e. At this time the spacecraft were located at (10.1,2.8,-0.4) Earth radii (GSE) and the magnetopause normal is approximately in the x-direction. Figure 1b shows that a southward reconnection jet reaching $\sim 150\,\text{km}\,\text{s}^{-1}$ is observed at the magnetopause crossing. The southward jet occurs in conjunction with an increased duskward flow. The electron density n_e increases across the magnetopause by an order of magnitude when the B_z reversal and ion outflow are observed. At the magnetopause boundary intense current densities $\mathbf{J}$ are observed with $|\mathbf{J}|$ peaking at $1500\,\text{nA}\,\text{m}^{-2}$, based on Curlometer [*Dunlop et al.*, 1988] from the four spacecraft (Figure 1d). Comparable current densities are observed parallel and perpendicular to $\mathbf{B}$. Based on timing analysis of B_z across the spacecraft we estimate the magnetopause speed to be $\approx 25\,\text{km}\,\text{s}^{-1}$ in the $-$x direction. The reversal in B_z then occurs over spatial scales comparable to two ion inertial lengths $d_i = c/\omega_{pi} \approx 36\,\text{km}$, where ω_{pi} is the ion plasma frequency in the magnetosheath. For reference, the magnetospheric ion inertial length $d_{i,MS}$

is $\approx 130\,\mathrm{km}$. Therefore, the current sheet is very narrow, consistent with the spacecraft crossing the magnetopause near the reconnection X line. Similarly, the southward outflow region has a width comparable to $2d_i$. Therefore, MMS crossed the magnetopause close to, but southward, of the reconnection X line.

Figures 1e and 1f show the omnidirectional ion and electron differential energy fluxes, respectively. The magnetosphere is characterized by hot (several keV) and intermediate ($\sim 1\,\mathrm{keV}$) energy ions, and relatively cold electrons (electron temperature $T_e \sim 40\,\mathrm{eV}$) with a high energy tail. The intermediate energy ions may be of magnetosheath origin, entering the magnetosphere from a distant reconnection site. Overall, there is little change in T_e as the spacecraft cross the magnetopause.

In Figures 1g and 1h we plot spectrograms of the ratios $f_{\|+}/f_{\|-}$ and $(f_{\|+} + f_{\|-})/2f_\perp$, where $f_{\|+}$, $f_{\|-}$, and $f_\perp$ are the electron phase-space densities parallel, antiparallel, perpendicular to $\mathbf{B}$, respectively, or equivalently at pitch angles $\theta = 0°$, $180°$, and $90°$. Comparable $f_{\|+}$ and $f_{\|-}$ are observed at the thermal energies of the distribution, except for after $\sim$05:16:00 UT. On the low density side of the magnetopause boundary the thermal electrons are heated parallel to $\mathbf{B}$, as seen in Figure 1h. Figure 1g shows that the differences between $f_{\|+}$ and $f_{\|-}$ are relatively small, indicating parallel heating rather than drifting electrons or electron beams aligned with $\mathbf{B}$. This heating is consistent with the electron heating observed on the magnetospheric inflow side of the X line [*Egedal et al.*, 2011; *Graham et al.*, 2014; *Lavraud et al.*, 2016]. We identify the ion diffusion region to be the blue shaded region in Figure 1, based on the observed electron heating and strong

perpendicular $\mathbf{J}$. Below we confirm that this is an ion diffusion region, where ions become demagnetized.

2.2. Ohm's law

We compare the observed electric fields in the ion diffusion region with the terms in Ohm's law. Ohm's law is given by

$$\mathbf{E} + \mathbf{V}_i \times \mathbf{B} = \frac{\mathbf{J} \times \mathbf{B}}{n_e q_e} - \frac{\nabla \cdot \mathbf{P}_e}{n_e q_e}, \tag{1}$$

where $\mathbf{E}$ is the electric field, q_e is the electron charge, and $\mathbf{P}_e$ is the electron pressure tensor. We calculate the Hall term $\mathbf{J} \times \mathbf{B}/n_e q_e$ and electron pressure term $\nabla \cdot \mathbf{P}_e/n_e q_e$ using four-spacecraft methods to estimate $\mathbf{J}$ and $\nabla \cdot \mathbf{P}_e$, and use the full electron pressure tensor in the calculation of $\nabla \cdot \mathbf{P}_e$. Therefore, we use the four-spacecraft average of the ion convection term $-\mathbf{V}_i \times \mathbf{B}$ and the observed $\mathbf{E}$ to directly compare the fields.

In Figure 2 we plot the observed $\mathbf{E}$ and the terms in equation (1). Figures 2a and 2b show $\mathbf{B}$ and $\mathbf{E}$ ($32\,\mathrm{s}^{-1}$ fast resolution) averaged over the four spacecraft. These fields do not include contributions from high-frequency waves. The electric field is primarily in the x-direction, reaching an amplitude close to $10\,\mathrm{mV\,m}^{-1}$. Figures 2c–2e show the Hall, convection, and electron pressure terms, respectively. The Hall term is in the x-direction and exceeds the amplitude of the observed $\mathbf{E}$. The convection and electron pressure terms are in the $-$x-direction, but have smaller amplitude than the Hall term. The deviation of the ion convection term from the observed $\mathbf{E}$ and the strong Hall term indicate that the ions have become demagnetized. The electron pressure term is produced by the density gradient at the magnetopause boundary (Figure 1c). The direction and relative

magnitude of these terms are consistent with observations and simulations of asymmetric reconnection [*Khotyaintsev et al.*, 2006; *Pritchett and Mozer*, 2009; *Malakit et al.*, 2013].

Figure 2f shows the electron convection electric field $-\mathbf{V}_e \times \mathbf{B}$. Overall, $-\mathbf{V}_e \times \mathbf{B}$ reproduces well the observed $\mathbf{E}$, including the more rapid fluctuations. Within the ion diffusion region the fields have the same qualitative features, except $-\mathbf{V}_e \times \mathbf{B}$ peaks at a slightly higher amplitude in the x-direction. This might be due to the contribution of the electron pressure term to the observed $\mathbf{E}$. In Figure 2g we plot the x and y components of the terms on the left-hand side and right-hand side of equation (1), $\mathbf{E}_{\mathrm{LHS}}$ and $\mathbf{E}_{\mathrm{RHS}}$, respectively. (The z components of each term in equation (1) remain small.) For the x component $\mathbf{E}_{\mathrm{LHS}}$ and $\mathbf{E}_{\mathrm{RHS}}$ agree and become large within the ion diffusion region, confirming that the ions are demagnetized. For the y components the amplitudes are smaller and often differ within the ion diffusion region. This may be due to small-scale currents, which are unresolved by the Curlometer method (discussed in the following subsection). Outside the ion diffusion region both terms remain close to zero, indicating that the ions are magnetized. We conclude that the ions become demagnetized in the ion diffusion region, whereas the electrons remain approximately frozen in. The relative strengths and directions of the ion convection, Hall, and electron pressure terms agree with simulations of asymmetric reconnection, and the observed $\mathbf{E}$ is primarily balanced by the Hall term.

2.3. Electron scale currents

In this section we investigate the currents that develop in the ion diffusion region. We calculate $\mathbf{J}$ from the FPI particle moments using

$$\mathbf{J} = q_e n_e \left(\mathbf{V}_i - \mathbf{V}_e \right), \tag{2}$$

where $\mathbf{V}_i$ and $\mathbf{V}_e$ are the ion and electron bulk velocities. We assume $n_e = n_i$, where n_i is the ion number density. In Figures 3b–3d we show the current densities J_x, J_y, and J_z in the x, y, and z directions, respectively, calculated for each spacecraft using equation (2). The current densities are maximal in the ion diffusion region, where the B_z reversal occurs (Figure 3a), and occur over a length scale comparable to d_i. We observe current sheets with widths comparable to a few electron inertial lengths $d_e = c/\omega_{pe} \approx 800\,\mathrm{m}$, where ω_{pe} is the electron plasma frequency in the magnetosheath, which are significantly smaller than the spacecraft separation and are therefore not resolved using Curlometer. The length scales indicated in Figure 3 correspond to the magnetopause boundary speed ($\approx 25\,\mathrm{km}$). Figure 3c shows that $\mathbf{J}$ peaks at $\approx 2500\,\mathrm{nA\,m^{-2}}$, about a factor of two larger than $\mathbf{J}$ calculated using Curlometer.

In Figures 3e–3g we plot the four-spacecraft average of $\mathbf{J}$ calculated from the particle moments $\mathbf{J}_{\mathrm{moms}}$ and $\mathbf{J}$ calculated using Curlometer $\mathbf{J}_{\mathrm{curl}}$. We find very good agreement between $\mathbf{J}_{\mathrm{moms}}$ and $\mathbf{J}_{\mathrm{curl}}$; both exhibit the same qualitative features in the ion diffusion region. The most significant difference between $\mathbf{J}_{\mathrm{moms}}$ and $\mathbf{J}_{\mathrm{curl}}$ is in the x-direction. Figure 3b shows that J_x differs significantly between the four spacecraft. This indicates that there are current structures with widths well below the spacecraft separation and explains the differences in $\mathbf{J}_{\mathrm{moms}}$ and $\mathbf{J}_{\mathrm{curl}}$ in the x-direction. Excellent agreement is found between $\mathbf{J}_{\mathrm{moms}}$ and $\mathbf{J}_{\mathrm{curl}}$ in the y- and z-directions. Similarly, we find excellent agreement between

$\mathbf{J}_{\mathrm{moms}}$ and $\mathbf{J}_{\mathrm{curl}}$ for the field-aligned currents (not shown, but follows from the agreement in the z-direction). This agreement is expected because the Curlometer method calculates the average current over the spacecraft tetrahedron, which should roughly equal $\mathbf{J}_{\mathrm{moms}}$ averaged over the four spacecraft. These results show that the particle moments used to calculate $\mathbf{J}_{\mathrm{moms}}$ are reliable.

In the ion diffusion region the electrons are approximately frozen in, whereas the ions are not frozen in. Therefore, we can estimate the perpendicular current density $\mathbf{J}_{\perp}$ as

$$\mathbf{J}_{\perp} = -q_e n_e \frac{\mathbf{E} \times \mathbf{B}}{|\mathbf{B}|^2}, \tag{3}$$

which corresponds to $\mathbf{E} \times \mathbf{B}$ drifting electrons and stationary ions. Figures 4a–4c show $J_{\perp x}$, $J_{\perp y}$, and $J_{\perp z}$ from MMS1 in the ion diffusion region (the length scales indicated in Figure 4b correspond to the magnetopause boundary speed). We compare $\mathbf{J}_{\perp}$ calculated from Curlometer, the particle moments, and equation (3) for fast and burst resolution $\mathbf{E}$, $\mathbf{J}_{\mathrm{Efast}}$ and $\mathbf{J}_{\mathrm{Ebrst}}$, respectively. Both $\mathbf{J}_{\mathrm{moms}}$ and $\mathbf{J}_{\mathrm{Efast}}$ show the same features, indicating that the perpendicular currents are carried by electrons. Thin current sheets are observed with thicknesses comparable to a few d_e, which are unresolved by $\mathbf{J}_{\mathrm{curl}}$.

The timeseries of $\mathbf{J}_{\mathrm{Ebrst}}$ shows more rapid fluctuations, which are unresolved by $\mathbf{J}_{\mathrm{Efast}}$ and $\mathbf{J}_{\mathrm{moms}}$. These fluctuations in $\mathbf{J}_{\mathrm{Ebrst}}$ are due to the electric field fluctuations of lower-hybrid drift waves produced at the density gradient [*Krall and Liewer*, 1971], which are under-resolved by $\mathbf{J}_{\mathrm{Efast}}$ and $\mathbf{J}_{\mathrm{moms}}$. To determine whether equation (3) remains valid for lower-hybrid drift waves we investigate the properties of the observed waves. Based on the local plasma conditions we predict that electrostatic lower-hybrid drift waves have $k_{\perp} \sim 1/\rho_e \sim 2 \times 10^{-3}\,\mathrm{m}^{-1}$, corresponding to a wavelength $\lambda_{\perp} \sim 3\,\mathrm{km}$, where ρ_e is the

electron gyroradius [*Davidson et al.*, 1977]. We estimate the phase speed to be $v = \omega_{LH}/k_\perp \sim 100\,\mathrm{km\,s^{-1}}$, where $\omega_{LH} \approx 200\,\mathrm{s^{-1}}$ is the angular lower-hybrid frequency. The spacecraft separations ($\approx 15\,\mathrm{km}$) are too large to find any correlations between **E** from different spacecraft, which suggests that the waves have wavelengths $\lambda_\perp < 15\,\mathrm{km}$, so we use the single spacecraft method developed in *Norgren et al.* [2012] to estimate the wave properties. *Norgren et al.* [2012] estimate the electrostatic potential of the wave to be

$$\phi_B = \frac{|\mathbf{B}|}{q_e n_e \mu_0} \delta B_\parallel, \tag{4}$$

where $\delta B_\parallel$ are the magnetic field fluctuations aligned with the background **B**. The phase velocity **v** is found by fitting the potential $\phi_E = \int \delta \mathbf{E} dt \cdot \mathbf{v}$ to ϕ_B, where $\delta \mathbf{E}$ is the fluctuating electric field. For lower-hybrid waves $\delta B_\parallel$, and hence ϕ_B, are produced by the currents associated with $\delta \mathbf{E} \times \mathbf{B}$ drifting electrons.

As an example Figures 4d and 4e show ϕ_B and ϕ_E calculated from MMS1 in the yellow shaded region with bandpass filtering for frequencies $10\,\mathrm{Hz} < f < 20\,\mathrm{Hz}$ and $f > 20\,\mathrm{Hz}$, respectively. In both cases ϕ_B and ϕ_E agree well with each other. For the $10\,\mathrm{Hz} < f < 20\,\mathrm{Hz}$ and $f > 20\,\mathrm{Hz}$ cases we estimate phase speeds v of $104\,\mathrm{km\,s^{-1}}$ and $67\,\mathrm{km\,s^{-1}}$, respectively, which are consistent with the predictions for electrostatic lower-hybrid waves. The waves propagate in the $-y$-direction along the magnetopause. The corresponding wavelengths are $\lambda_\perp \approx 10\,\mathrm{km}$ and $\lambda_\perp \approx 3.5\,\mathrm{km}$, which are larger than the local $\rho_e \approx 600\,\mathrm{m}$ and $d_e \approx 1.3\,\mathrm{m}$, but significantly smaller than ion spatial scales. The agreement between ϕ_B and ϕ_E, as well as the agreement between the estimated and predicted v are consistent with electrons remaining magnetized. In particular, Figure 4e shows that electrons can remain magnetized for observed frequencies that are unresolved by FPI

and fast mode $\mathbf{E}$. The rapid fluctuations in $\mathbf{J}_{\mathrm{Ebrst}}$ then correspond to lower-hybrid drift waves with significantly larger speeds than the magnetopause boundary speed. Therefore, equation (3) should remain valid at lower-hybrid wave frequencies and $\mathbf{J}_{\mathrm{Ebrst}}$ corresponds to current densities, which are under-resolved by $\mathbf{J}_{\mathrm{Efast}}$ and $\mathbf{J}_{\mathrm{moms}}$. More generally, we observe similar fluctuations in $\mathbf{J}_{\mathrm{Ebrst}}$ on each spacecraft. The largest $\mathbf{J}_{\mathrm{Ebrst}}$ observed peaks at $4000\,\mathrm{nA\,m^{-2}}$ on MMS2. We also estimate similar properties for the lower-hybrid drift waves on each spacecraft. The fluctuations in $\mathbf{B}$ associated with the lower-hybrid drift waves are substantially smaller than the differences in $\mathbf{B}$ between the spacecraft, so the waves do not contribute significantly to $\mathbf{J}$ calculated using Curlometer. We conclude that the large-amplitude fluctuations in $\mathbf{J}_{\mathrm{Ebrst}}$ are due to the electron motion associated with lower-hybrid drift waves, as well as larger-scale DC electric fields moving with the magnetopause boundary.

2.4. Electron heating

In this section we argue that the parallel heating observed in Figure 1 is consistent with trapping and acceleration by parallel electric fields near the X line. Figures 5a and 5b show electron pitch-angle distributions outside and inside the ion diffusion region, respectively. Outside the ion diffusion region there is only a small increase in electron fluxes near pitch angles $\theta = 0°$ and $180°$. Within the ion diffusion region the electron fluxes near $\theta = 0°$ and $180°$ are significantly enhanced at thermal energies. These distributions correspond to the enhanced $(f_{\|+} + f_{\|-})/2f_{\perp}$ observed in Figure 1h. Figure 5c shows the phase-space density $f_e(E)$ of the pitch-angle distribution. The distribution is characterized by electron heating parallel to $\mathbf{B}$ and a flat-top distribution for $E \lesssim 200\,\mathrm{eV}$ at $\theta = 0°$ and $180°$, which

are characteristic features of the inflow region near the ion diffusion region [*Egedal et al.*, 2008]. The higher energy magnetospheric electrons around $E \sim 1\,\mathrm{keV}$ are more isotropic.

We now estimate the parallel accelerating potential $\Phi_{\parallel}$ associated with large-scale parallel electric fields that is required to produce the observed electron distributions [*Egedal et al.*, 2008]. For regions with $\Phi_{\parallel} > 0$ electrons can become trapped and passing electrons are accelerated, which produces electron heating parallel to $\mathbf{B}$ and flat-top distributions parallel and antiparallel to $\mathbf{B}$. For $\Phi_{\parallel} < 0$ electrons are reflected, which reduces the density. For constant $|\mathbf{B}|$ the distribution at $\theta = 90°$ remains unchanged for $\Phi_{\parallel} > 0$. The observed electron heating develops prior to the B_z reversal and $|\mathbf{B}|$ changes little from the background magnetospheric value, so for magnetospheric electrons we expect the effect of changes in $|\mathbf{B}|$ to be negligible. Likewise, the electron temperatures $T_{e\perp}$ perpendicular to $\mathbf{B}$ on each spacecraft change little across the magnetopause. Therefore, to estimate the $\Phi_{\parallel}$ required to reproduce the observed distributions we assume an isotropic distribution equal to the observed distribution at $\theta = 90°$, which should provide a reasonable approximation to the background distribution. We fit a Maxwellian to the observed distribution at $\theta = 90°$ for $E \lesssim 400\,\mathrm{eV}$, then use Liouville's theorem to find the value of $\Phi_{\parallel}$ required to reproduce the observed distributions at $\theta = 0°$ and $180°$. As an example we plot the fits to the observed $f_e(E)$ in Figure 5c; $\Phi_{\parallel} \approx 180\,\mathrm{V}$ is required to reproduce the observed $f_e(E)$, consistent with previous observations at the magnetopause [*Graham et al.*, 2014]. In Figure 5c a second Maxwellian is used to model the higher energy electrons and shows that these electrons are too energetic to be significantly affected by $\Phi_{\parallel}$, so superthermal electrons are not significantly heated. Therefore, the observed distribution is consistent

with electron trapping and acceleration by large-scale parallel electric fields. Below we use an automated fitting routine to estimate $\Phi_\parallel$ for each electron distribution in the diffusion region on each spacecraft.

Figure 5g shows $\Phi_\parallel$ estimated from each electron distribution in the diffusion region. Each spacecraft shows a similar timeseries of $\Phi_\parallel$, with $\Phi_\parallel$ peaking at approximately 180 V on MMS1. The peaks in $\Phi_\parallel$ on each spacecraft are observed at relatively low n_e and $\Phi_\parallel$ decreases as n_e increases across the magnetopause. The profiles of $\Phi_\parallel$ are similar except for the time offsets, indicating a spatial structure. Based on timing analyses between the spacecraft we estimate that the region of enhanced $\Phi_\parallel$ moves at $\approx 30\,\mathrm{km\,s^{-1}}$ in the $-$x-direction, consistent with it moving with the magnetopause boundary. Moreover, the spatial scale of the enhanced $\Phi_\parallel$ is comparable to $2d_i$, consistent with simulations [*Egedal et al.*, 2011]. We find that $\Phi_\parallel/T_e$ peaks at ≈ 3 on each spacecraft, which is comparable to the ratio of the parallel to perpendicular electron pressure $P_\parallel/P_\perp$ (Figure 5h). Based on the asymptotic scalings for electron trapping, equations (27)–(29) of *Egedal et al.* [2013], we predict $\Phi_\parallel \sim 200\,\mathrm{V}$ and $P_\parallel/P_\perp \sim 4$, consistent with the observed peaks in $\Phi_\parallel$ and $P_\parallel/P_\perp$. By comparing Figures 5g and 5h with Figure 5d we see that $\Phi_\parallel$ and $P_\parallel/P_\perp$ peak when the parallel current density $J_\parallel$ is negligible, which is expected because comparable $f_e(E)$ at $\theta = 0°$ and $180°$ are predicted and observed. Similarly, the large perpendicular current density $J_\perp$, which supports the observed Hall electric field, develops after the maximal $\Phi_\parallel$. Therefore, the electron heating develops in the inflow region prior to the steepest density gradients, and the strongest Hall electric field in Figure 2b.

In Figure 5i we plot $|\delta \mathbf{E}|$ from each spacecraft, which are associated with the lower-hybrid drift waves; the DC Hall electric fields have much lower amplitude. The lower-hybrid waves develop in the diffusion region and are most intense at the sharpest density gradient. The most intense lower-hybrid drift waves are observed after the peaks in $\Phi_\parallel$ and $P_\parallel/P_\perp$, and no correlation between the amplitudes of $\Phi_\parallel$ and $|\delta \mathbf{E}|$ is observed. This suggests that the lower-hybrid drift waves are unlikely to explain the observed electron heating. Indeed, $\Phi_\parallel$ and $P_\parallel/P_\perp$ are maximal when $|\delta \mathbf{E}|$ is relatively small on each spacecraft. In Figure 5j we plot $|\phi_B|$ calculated using equation (4) to estimate the potentials of the lower-hybrid drift waves. The maximum $|\phi_B|$ is $\approx 20\,\mathrm{V}$, which can potentially scatter electrons, but is much smaller than the estimated $\Phi_\parallel$. Although $|\phi_B|$ only becomes significant within the ion diffusion region, the peaks in $|\phi_B|$ are not well correlated with the peaks in $\Phi_\parallel$ and $P_\parallel/P_\perp$. Therefore, we conclude that the electrons are primarily heated by large-scale fields, rather than the lower-hybrid drift waves. The primary effect of the lower-hybrid drift waves is to produce large-amplitude currents due to the electron motion associated with the wave.

The results presented here confirm the observations by *Graham et al.* [2014] of the ion diffusion region, viz., the parallel electron heating is consistent with electron trapping by parallel electric fields, rather than heating by lower-hybrid drift waves. The most significant difference is that here the magnetosphere and magnetosheath have comparable T_e near the diffusion region, so both magnetospheric and magnetosheath electrons can be trapped in the diffusion region. By using multi-spacecraft observations at close separations and the significantly improved time resolution of FPI we are able to show that the electron

heating is a spatial feature of the ion diffusion region, and develops toward the inflow region prior to the strongest Hall electric field, current densities, and the most intense lower-hybrid drift waves. This supports the interpretation that the electron heating is produced by large-scale parallel electric fields rather than wave-particle interactions, which would likely differ on each spacecraft. For instance, the largest electric field fluctuations and $|\phi_B|$ are observed by MMS2, but there is no associated increase in $P_\parallel/P_\perp$. We conclude that the observed electron heating is consistent with electron trapping and acceleration by large-scale parallel electric fields, rather than wave-particle interactions.

3. Conclusions

In this letter we have investigated the structure of the ion diffusion region of asymmetric reconnection at Earth's magnetopause. The ion diffusion region is characterized by strong electron currents parallel and perpendicular to $\mathbf{B}$, a strong DC electric field in the normal direction, which is approximately equal to the Hall electric field, electron heating parallel to $\mathbf{B}$, and intense lower-hybrid drift waves.

The key results of this letter are:

(1) Current sheets well below ion spatial scales occur in the ion diffusion region, which are unresolved by Curlometer even at small spacecraft separations of $\sim 15\,\mathrm{km}$. Both the parallel and perpendicular currents are carried by electrons in the ion diffusion region. Electron motion associated with lower-hybrid drift waves produces large fluctuations in the current density.

(2) Parallel electron heating is observed in the ion diffusion region and is offset in position toward the magnetospheric inflow region from the Hall electric field and the

largest current densities. The electron heating is consistent with electron trapping by parallel electric fields rather than wave-particle interactions, in particular, heating by lower-hybrid drift waves.
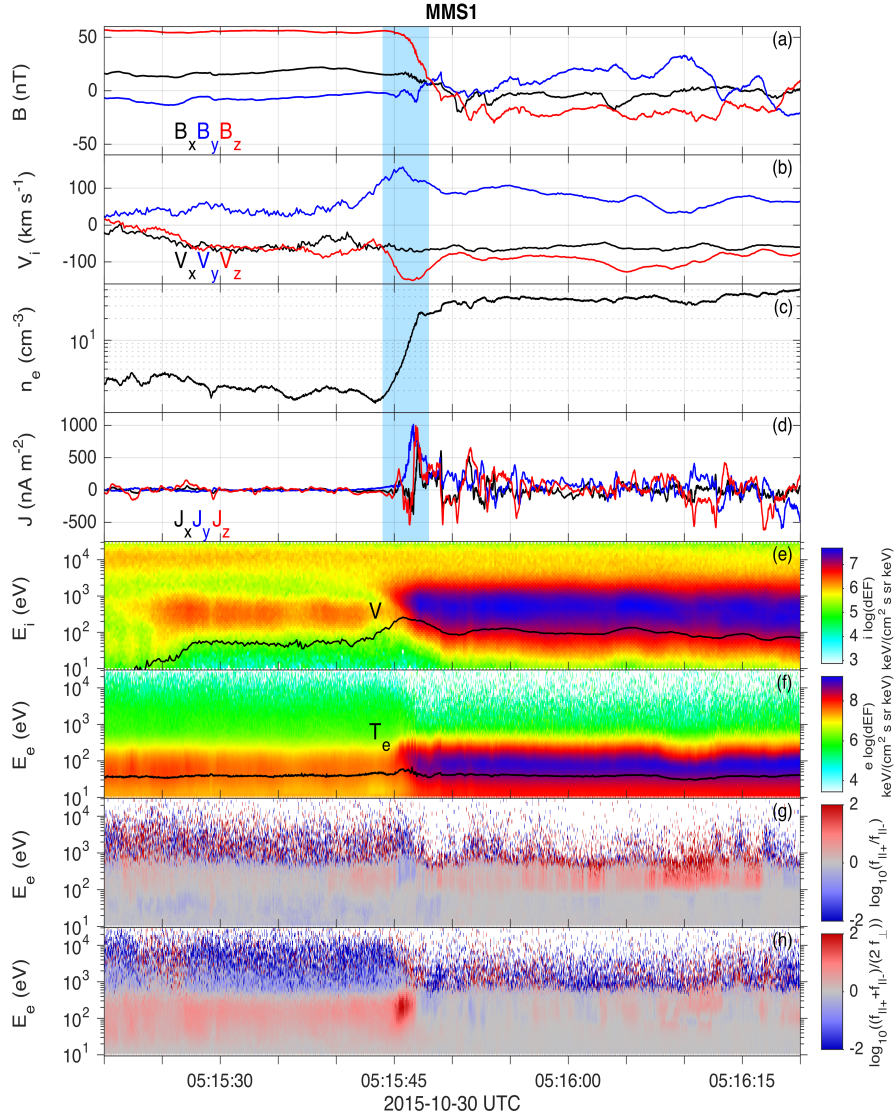
References

Bale, S. D., F. S. Mozer, and T. Phan (2002), Observation of lower hybrid drift instability in the diffusion region at a reconnecting magnetopause, *Geophys. Res. Lett.*, *29*, 2180, doi:10.1029/2002GL016113.

Burch, J. L., T. E. Moore, R. B. Torbert, and B. L. Giles (2015), Magnetospheric multiscale overview and science objectives, *Space Sci. Rev.*, pp. 1–17, doi:10.1007/s11214-015-0164-9.

Cairns, I. H., and B. F. McMillan (2005), Electron acceleration by lower hybrid waves in magnetic reconnection regions, *Phys. Plasmas*, *12*, 102,110, doi:10.1063/1.2080567.

Chen, L.-J., et al. (2008), Evidence of an extended electron current sheet and its neighboring magnetic island during magnetotail reconnection, *J. Geophys. Res.*, *113*, A12,213, doi:10.1029/2008JA013385.

Davidson, R. C., N. T. Gladd, C. S. Wu, and J. D. Huba (1977), Effects of finite plasma beta on the lower-hybrid-drift instability, *Phys. Fluids*, *20*, 301, doi:10.1063/1.861867.

Dunlop, M. W., D. J. Southwood, K.-H. Glassmeier, and F. M. Neubauer (1988), Analysis of multipoint magnetometer data, *Advances in Space Research*, *8*, 273, doi: 10.1016/0273-1177(88)90141-X.

Egedal, J., W. Fox, N. Katz, M. Porkolab, M. Oieroset, R. P. Lin, W. Daughton, and J. F. Drake (2008), Evidence and theory for trapped electrons in guide field magnetotail reconnection, *J. Geophys. Res.*, *113*, A12,207, doi:10.1029/2008JA013520.

Egedal, J., A. Le, P. L. Pritchett, and W. Daughton (2011), Electron dynamics in two-dimensional asymmetric anti-parallel reconnection, *Phys. Plasmas*, *18*, 102,901, doi: 10.1063/1.3646316.

Egedal, J., A. Le, and W. Daughton (2013), A review of pressure anisotropy caused by electron trapping in collision less plasma, and its implications for magnetic reconnection, *Phys. Plasmas*, *20*, 061,201, doi:10.1063/1.4811092.

Ergun, R. E., et al. (2014), The axial double probe and fields signal processing for the MMS mission, *Space Sci. Rev.*, pp. 1–22, doi:10.1007/s11214-014-0115-x.

Graham, D. B., Y. V. Khotyaintsev, A. Vaivads, M. André, and A. N. Fazakerley (2014), Electron dynamics in the diffusion region of an asymmetric magnetic reconnection, *Phys. Rev. Lett.*, *112*, 215,004, doi:10.1103/PhysRevLett.112.215004.

Khotyaintsev, Y. V., A. Vaivads, A. Retinò, M. André, C. J. Owen, and H. Nilsson (2006), Formation of inner structure of a reconnection separatrix region, *Phys. Rev. Lett.*, *97*, 205,003, doi:10.1103/PhysRevLett.97.205003.

Krall, N. A., and P. C. Liewer (1971), Low-frequency instabilities in magnetic pulses, *Phys. Rev. A*, *4*, 2094, doi:10.1103/PhysRevA.4.2094.

Lavraud, B., et al. (2016), Currents and associated electron scattering and bouncing near the diffusion region at Earth's magnetopause, *Geophys. Res. Lett.*, *43*, doi: 10.1002/2016GL068359.

Le Contel, O., et al. (2014), The search-coil magnetometer for MMS, *Space Sci. Rev.*, pp. 1–26, doi:10.1007/s11214-014-0096-9.

Lindqvist, P.-A., et al. (2014), The Spin-Plane Double Probe electric field instrument for MMS, *Space Sci. Rev.*, pp. 1–29, doi:10.1007/s11214-014-0116-9.

Malakit, K., M. A. Shay, P. A. Cassak, and D. Ruffolo (2013), New electric field in asymmetric magnetic reconnection, *Phys. Rev. Lett.*, *111*, 135,001, doi: 10.1103/PhysRevLett.111.135001.

Mozer, F. S., P. L. Pritchett, J. Bonnell, D. Sundkvist, and M. T. Chang (2008), Observations and simulations of asymmetric magnetic field reconnection, *J. Geophys. Res.*, *113*, A00C03, doi:10.1029/2008JA013535.

Norgren, C., A. Vaivads, Y. V. Khotyaintsev, and M. Andre (2012), Lower hybrid drift waves: Space observations, *Phys. Rev. Lett.*, *109*, 055,001, doi: 10.1103/PhysRevLett.109.055001.

Pollock, C., et al. (2016), Fast plasma investigation for magnetospheric multiscale, *Space Sci. Rev.*, pp. 1–76, doi:10.1007/s11214-016-0245-4.

Pritchett, P. L. (2013), The influence of intense electric fields on three-dimensional asymmetric magnetic reconnection, *Phys. Plasmas*, *20*, 061,204, doi:10.1063/1.4811123.

Pritchett, P. L., and F. S. Mozer (2009), Asymmetric magnetic reconnection in the presence of a guide field, *J. Geophys. Res.*, *114*, A11,210, doi:10.1029/2009JA014343.

Roytershteyn, V., W. Daughton, H. Karimabadi, and F. S. Mozer (2012), Influence of the

    lower-hybrid drift instability on magnetic reconnection in asymmetric configurations,

    Phys. Rev. Lett., *108*, 185,001, doi:10.1103/PhysRevLett.108.185001.

Russell, C. T., et al. (2014), The magnetospheric multiscale magnetometers, *Space Sci.*

    Rev., pp. 1–68, doi:10.1007/s11214-014-0057-3.

Tanaka, K. G., et al. (2008), Effects on magnetic reconnection of a density asymmetry

    across the current sheet, *Ann. Geophys.*, *26*, 2471, doi:10.5194/angeo-26-2471-2008.

Vaivads, A., Y. Khotyaintsev, M. André, A. Retino, S. C. Buchert, B. N. Rogers, P. De-

    creau, G. Paschmann, and T. D. Phan (2004a), Structure of the magnetic reconnection

    diffusion region for four-spacecraft observations, *Phys. Rev. Lett.*, *93*, 105,001, doi:

    10.1103/PhysRevLett.93.105001.

Vaivads, A., M. André, S. C. Buchert, J.-E. Wahlund, A. N. Fazakerley, and N. Cornilleau-

    Wehrlin (2004b), Cluster observations of lower hybrid turbulence within thin layers at

    the magnetopause, *Geophys. Res. Lett.*, *31*, L03,804, doi:10.1029/2003GL018142.

Figure 1. The magnetopause crossing observed on 30 October 2015 by MMS1. (a) **B**. (b) Ion velocity $\mathbf{V}_i$. (c) n_e. (d) C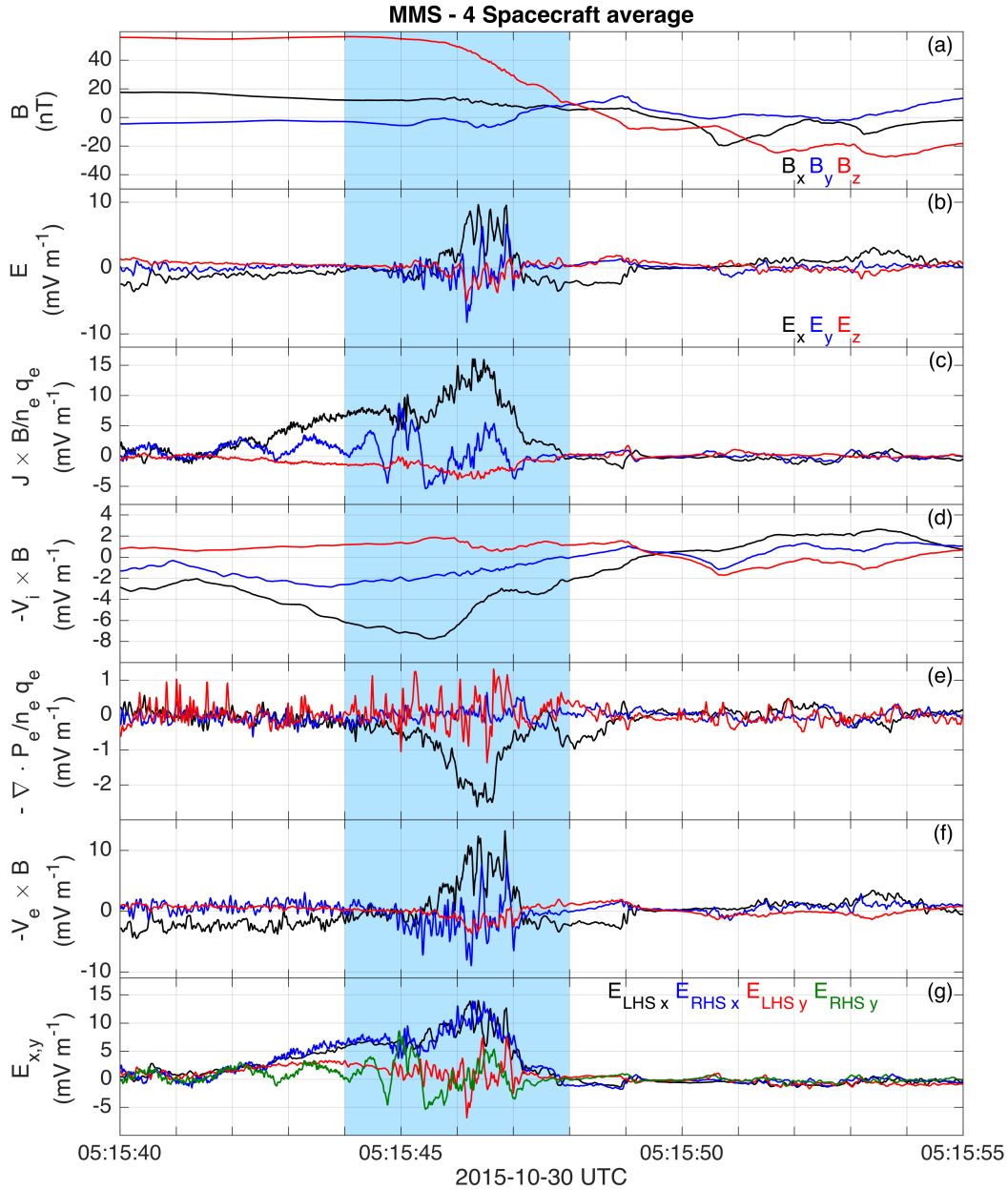urrent density $\mathbf{J}$ calculated using Curlometer. (e) Omnidirectional ion differential energy flux (the black line is the energy corresponding to the ion speed V_i). (f) Omnidirectional electron differential energy flux (the black line is T_e). (g) The ratio of parallel to antiparallel electron phase-space density $f_{\parallel+}/f_{\parallel-}$. (h) Ratio of parallel to perpendicular electron phase-space density $(f_{\parallel+} + f_{\parallel-})/2f_{\perp}$. The blue shaded region indicates the ion diffusion region.
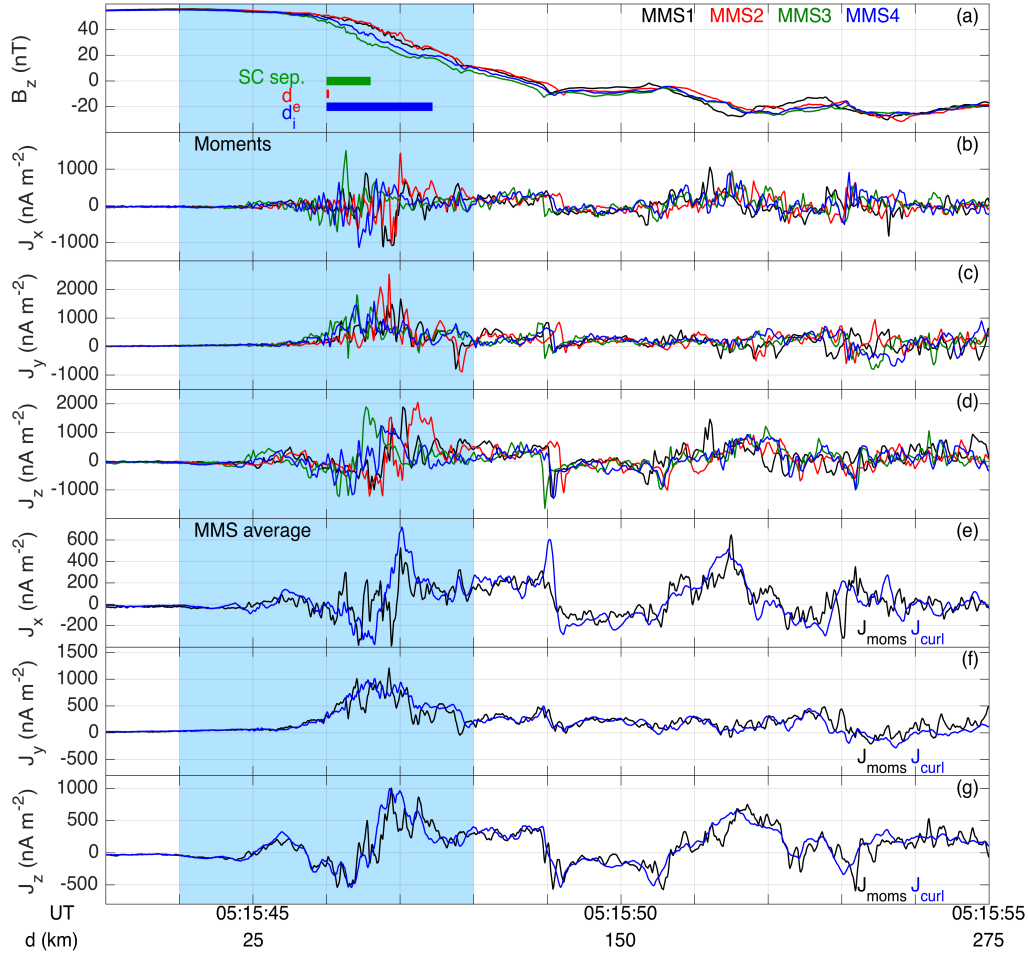
Figure 2.   Four spacecraft averages of the electric fields observed in the ion diffusion region. (a) **B**, (b) **E** observed at fast sampling frequency, (c)–(e) Hall, ion convection, and electron pressure terms. (f) Electron convection electric field. (g) The x and y components of the left-hand side and right-hand side of equation (1). The blue shaded region indicates the ion diffusion region.
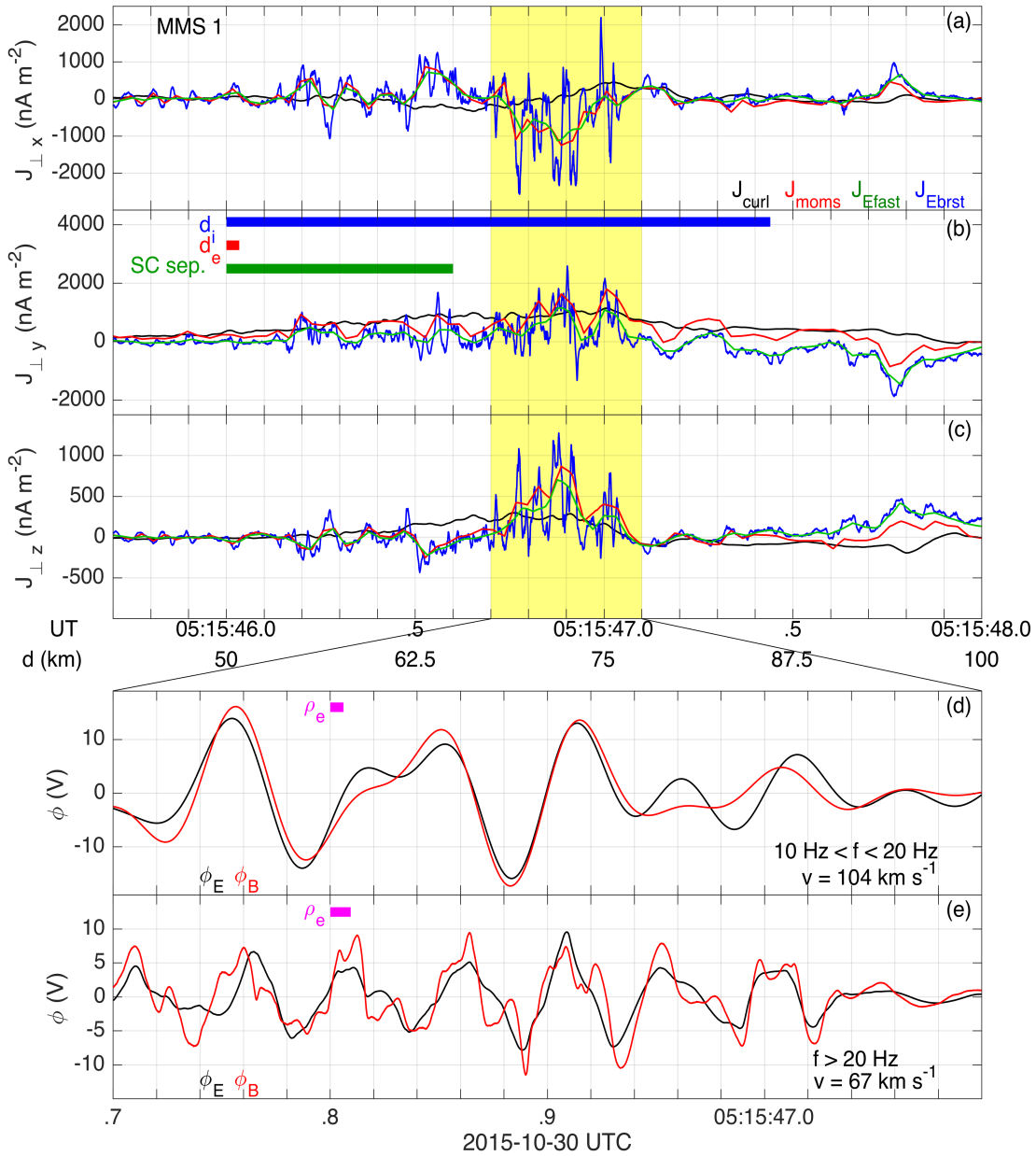
Figure 3. Current densities calculated from the particle moments and Curlometer over the magnetopause crossing. (a) B_z from each spacecraft. (b)–(d) Current densities J_x, J_y, and J_z calaculated from the particle moments in the x, y, and z-directions, respectively. (e)–(g) Four-spacecraft average of the current density $\mathbf{J}_{\text{moms}}$ computed from the particle moments and current density calculated from Curlometer $\mathbf{J}_{\text{curl}}$ in the x, y, and z directions, respectively. The thick blue, red, and green lines in (a) indicate d_i, d_e, and the spacecraft separation, respectively. The blue shaded region indicates the ion diffusion region.
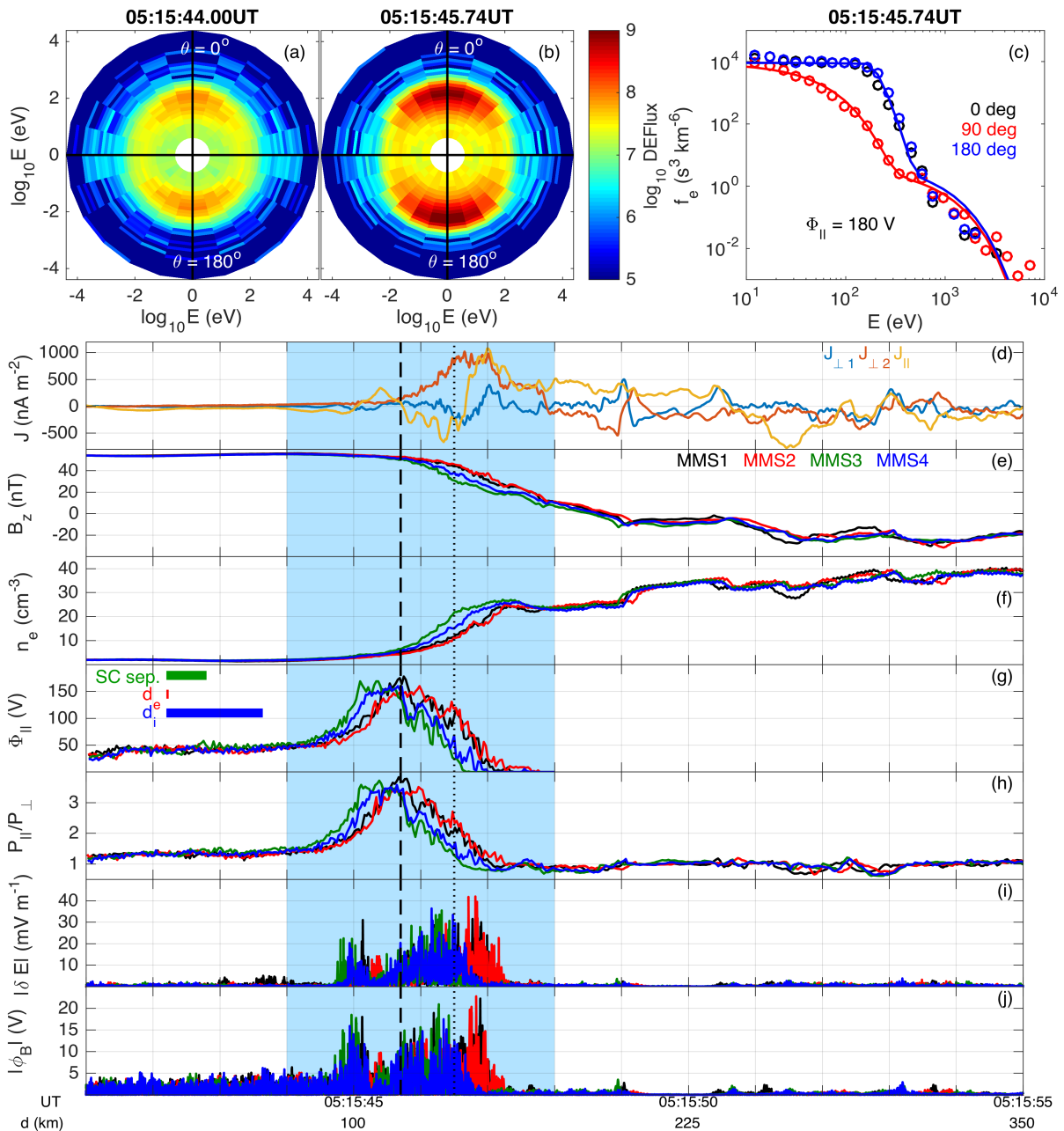
Figure 4. Perpendicular current densities $\mathbf{J}_\perp$ observed in the ion diffusion region by MMS1. $\mathbf{J}_\perp$ is calculated using Curlometer (black), particle moments (red), equation (3) using fast mode $\mathbf{E}$ (green), and equation (3) using burst mode $\mathbf{E}$ (blue). Panels (a)–(c) are timeseries of $\mathbf{J}_\perp$ in the x, y, and z directions, $J_{\perp x}$, $J_{\perp y}$, and $J_{\perp z}$, respectively. The thick blue, red, and green lines in (b) indicate d_i, d_e, and the spacecraft separation, respectively. Panels (d) and (e) show ϕ_E (black) and ϕ_B (red) for the lower-hybrid drift waves observed in the yellow shaded region in (a)–(c) for bandpasses $10\,\mathrm{Hz} < f < 20\,\mathrm{Hz}$ and $f > 20\,\mathrm{Hz}$,

respectively. The thick magenta lines indicate the local ρ_e.

Figure 5. Parallel electron heating observed in the ion diffusion region. (a) and (b) Electron pitch-angle distributions outside and inside the ion diffusion region observed by MMS1. (c) Electron phase-space density of the distribution in (b) at pitch angles 0°, 90° and 180° (circles) and fit to the data (solid lines). Panel (d) shows the timeseries of **J** in field-aligned coordinates calculated using Curlometer. Panels (e)–(j) show timeseries of B_z, n_e, $\Phi_\parallel$, $P_\parallel/P_\perp$, $|\mathbf{E}|$, and $|\phi_B|$ for each spacecraft, respectively. The thick blue, red, and green lines in (g) indicate d_i, d_e, and the spacecraft separation, respectively. The dashed and dotted vertical lines indicate the approximate times the parallel electron heating and Hall electric field are maximal, respectively. The blue shaded region indicates the ion diffusion region.